



# A high efficient photocatalyst $\text{Ag}_3\text{VO}_4/\text{TiO}_2$ /graphene nanocomposite with wide spectral response

Jinxu Wang, Peixian Wang, Yuantao Cao, Jing Chen, Wenjuan Li, Yu Shao, Yi Zheng, Danzhen Li\*

Research Institute of Photocatalysis, State Key Laboratory Breeding Base of Photocatalysis, Fuzhou University, Fuzhou 350002, PR China



## ARTICLE INFO

### Article history:

Received 2 December 2012

Received in revised form 27 January 2013

Accepted 3 February 2013

Available online 13 February 2013

### Keywords:

Visible light photocatalyst

$\text{Ag}_3\text{VO}_4$

$\text{TiO}_2$

Graphene

Heterojunction

## ABSTRACT

Great efforts have been made to develop efficient visible light activated photocatalysts in recent years. In this work,  $\text{Ag}_3\text{VO}_4/\text{TiO}_2$ /graphene nanocomposite as a wide spectrum responsive photocatalyst was prepared first by a two-step process, which exhibited obviously increased visible light absorption and photocatalytic activity in degradation of organic pollutants including methyl orange and Rhodamine B, compared with  $\text{Ag}_3\text{VO}_4/\text{TiO}_2$  and  $\text{TiO}_2/\text{GR}$  nanocomposites. For  $\text{Ag}_3\text{VO}_4/\text{TiO}_2$ /graphene nanocomposite, the introduction of graphene contributed to the uniform dispersion of  $\text{Ag}_3\text{VO}_4$  and  $\text{TiO}_2$  nanoparticles on graphene sheets. The capacity of graphene in storing and shuttling electrons and the formation of heterojunction between  $\text{Ag}_3\text{VO}_4$  and  $\text{TiO}_2$  facilitated together the enhancement of efficiency in the separation of photogenerated electron–hole pairs. Based on the results of photoelectrochemical measurement and the detection of active species in photocatalytic degradation process, the transfer of photogenerated carriers and photocatalytic degradation mechanism on  $\text{Ag}_3\text{VO}_4/\text{TiO}_2$ /graphene nanocomposite were proposed and discussed in detail.

© 2013 Elsevier B.V. All rights reserved.

## 1. Introduction

Heterogeneous photocatalysis by use of semiconductor materials has been applied as an efficient method in the field of environmental purification.  $\text{TiO}_2$  nanoparticle photocatalysts are generally believed to be the most reliable material for the degradation of organic compounds due to their non-toxicity, low cost, physical and chemical stability and high reactivity [1,2]. Sun light radiation consists of about 5% UV light, 47% visible light and 48% infrared radiation. Unfortunately,  $\text{TiO}_2$  as the benchmark of UV photocatalysts is inactive under visible light due to its wide band gap [3]. Moreover, the photogenerated electrons and holes in the excited states playing a very important role in pollutant degradation are unstable and can be easily recombined, which results in low efficiency of photocatalysis [4]. Therefore,  $\text{TiO}_2$  cannot make use of the vast potential of solar photocatalysis.

Up to now, a variety of strategies have been employed to narrow its band gap and enhance the visible light photocatalytic performance via either doping [5–9] or modification [10–12] or semiconductor coupling [13–18]. Coupling of  $\text{TiO}_2$  with narrow band gap semiconductors as sensitizers which are capable of absorbing visible light has been proved to be a feasible approach.

In recent years, tremendous efforts including the work of our team have been devoted to the formation of heterojunction between  $\text{TiO}_2$  and narrow band gap semiconductors to develop visible light responding photocatalyst with high activity [19–21]. The formation of heterojunction between  $\text{TiO}_2$  and a narrow band gap semiconductor with a more negative conducting band (CB) level can result in the injection of CB electrons from narrow band gap semiconductor to  $\text{TiO}_2$ , which is helpful for electron–hole separation [22–24]. However, for the design of highly efficient heterojunction photocatalyst, besides the demand of a commonsensible matching ability of band potentials between semiconductors, the smooth and spatially available transfer of charge (electron and hole) at the interface and the high electron and hole mobility of the semiconductors are significant to increase the photocatalytic activity [25]. For some heterojunction photocatalyst materials prepared by common wet chemical methods, the low proportion of effective structural elements with intimate contact interface and the high degree of lattice mismatch between two semiconductors decrease the efficiency of the transfer and separation of photogenerated carriers (electron and hole).

The introduction of graphene provides a feasible approach to solve the problem to some extent. Recently, functionalized graphene-based semiconductor photocatalysts have attracted a lot of attention due to their high electron conductivity, large specific surface area and adsorption [26]. Many efforts are put into the synthesis of  $\text{TiO}_2$ –graphene nanocomposite [27–29]. Benefiting

\* Corresponding author. Tel.: +86 591 83779256; fax: +86 591 83779256.  
E-mail addresses: [dzli@fzu.edu.cn](mailto:dzli@fzu.edu.cn), [danzli@126.com](mailto:danzli@126.com) (D. Li).

from the high specific surface area, graphene emerged as a good support to make the loaded nanoparticles to achieve a uniform distribution without aggregation [27]. The enhancement of photocatalytic activity for  $\text{TiO}_2$ -graphene nanocomposite is ascribed to the giant two-dimensional planar graphene structure favouring dye absorption, and suppressed electron-hole recombination due to the high electrical conductivity [30]. Furthermore, incorporation of two or more catalyst particles onto an individual graphene sheet at separate sites can provide greater versatility in carrying out selective catalytic or sensing processes and modify the structure and morphology of photocatalysts to enhance their photocatalytic performances [31–35].

In this study, incorporation of  $\text{Ag}_3\text{VO}_4$  with narrow gap band (2.2 eV) [36] and  $\text{TiO}_2$  onto graphene sheet was carried out firstly to obtain  $\text{Ag}_3\text{VO}_4/\text{TiO}_2/\text{graphene}$  nanocomposite. The composite of  $\text{Ag}_3\text{VO}_4$  and  $\text{TiO}_2$  semiconductors with appropriate oxidation reduction energy levels could enhance the charge separation by the formation of heterojunction between them and engender its wide spectral response by extension of light absorption to the visible region. The introduction of graphene as a good support made the loaded  $\text{Ag}_3\text{VO}_4$  and  $\text{TiO}_2$  nanoparticles achieve a uniform distribution and further enhanced the charge separation and suppressed electron-hole recombination. The expected enhanced photocatalytic activity of  $\text{Ag}_3\text{VO}_4/\text{TiO}_2/\text{graphene}$  nanocomposite was tested by degradation of organic pollutants (methyl orange and Rhodamine B). The photocatalytic mechanism for degradation of organic pollutants on  $\text{Ag}_3\text{VO}_4/\text{TiO}_2/\text{graphene}$  was discussed in detail.

## 2. Experiment

### 2.1. Preparation

#### 2.1.1. Synthesis of graphene oxide (GO)

GO nanosheets were prepared by chemical exfoliation of purified natural graphite powder by using a modified Hummers and Offeman method [37,38]. The concrete procedure of preparation was as follows. Firstly, 10 g of graphite powder (supplied by Qingdao Haida Graphite CO., Ltd., China) was added to the cooled ( $0^\circ\text{C}$ ) mixture of 230 mL of concentrated  $\text{H}_2\text{SO}_4$  and 60 mL of concentrated  $\text{HNO}_3$  under vigorous mechanical stirring. Secondly, 30 g  $\text{KMnO}_4$  was slowly added with stirring and the temperature of above mixture was to be cooled below  $20^\circ\text{C}$  by an external ice bath. Successively, the mixture was stirred at  $35^\circ\text{C}$  for 2 h. Thirdly, 500 mL of distilled water was slowly added to the mixture, resulting that the temperature increased to  $98^\circ\text{C}$  and maintained at the temperature for 30 min. Finally, 1.4 L water was poured quickly into the system so as to terminate the reaction and 20 mL 10% hydrogen peroxide was added to reduce the residual permanganate and manganese dioxide. The suspension was separated and washed repeatedly by centrifugation with 5% HCl solution and water to remove sulfate. The products were dialyzed for a week and dried in a vacuum oven at  $60^\circ\text{C}$  to obtain the relatively pure GO.

#### 2.1.2. Synthesis of $\text{TiO}_2/\text{graphene}$ ( $\text{TiO}_2/\text{GR}$ )

40 mg of GO was dispersed in 15 mL of absolute alcohol by ultrasound and stirring to obtain brown suspension which is poured into a 50 mL Teflon-lined stainless autoclave. Then, 5 mL of titanium tetrabutoxide ( $\text{Ti}(\text{OC}_4\text{H}_9)_4$ ) was added to the autoclave and the mixture was stirred for 1 h. After that, 1 mL of concentrated hydrochloric acid was added dropwise to the above mixture. Finally, the autoclave underwent a hydrothermal process at  $180^\circ\text{C}$  for 36 h, followed by cooling down to room temperature naturally. The products were harvested by centrifugation and washed several times with a mixture of ethanol and deionized water. After drying

in air at  $60^\circ\text{C}$  for 12 h, the  $\text{TiO}_2/\text{graphene}$  ( $\text{TiO}_2/\text{GR}$ ) nanocomposite was obtained. Pure  $\text{TiO}_2$  also can be prepared by the same method in the absence of GO.

#### 2.1.3. Synthesis of $\text{Ag}_3\text{VO}_4/\text{TiO}_2/\text{graphene}$ ( $\text{Ag}_3\text{VO}_4/\text{TiO}_2/\text{GR}$ )

0.1598 g of  $\text{TiO}_2/\text{GR}$  powder was dispersed in 60 mL of 12.5 M  $\text{AgNO}_3$  solution by ultrasound for 1 h and stirring for 1.5 h. Then, 20 mL of 12.5 M  $\text{NH}_4\text{VO}_3$  was poured into the suspension and 2 M NaOH was used to adjust the pH value of the whole system to 9. After stirring at 800 rpm for 2 h, the product was centrifuged and washed with distilled water for several times. The final solid product was slightly dried by cool air and then completely dried at  $60^\circ\text{C}$  for 12 h to obtain  $\text{Ag}_3\text{VO}_4/\text{TiO}_2/\text{GR}$  nanocomposite.  $\text{Ag}_3\text{VO}_4/\text{TiO}_2$  composite was gained when the  $\text{TiO}_2/\text{GR}$  was replaced by  $\text{TiO}_2$  in the above synthesis procedure.  $\text{Ag}_3\text{VO}_4$  was obtained in the absence of  $\text{TiO}_2/\text{GR}$  by the same method.

### 2.2. Characterization

X-ray diffraction (XRD) patterns were measured by a Bruker D8 Advance X-ray diffractometer at 40 kV and 40 mA with Ni-filtered  $\text{Cu K}\alpha$  radiation. Laser Raman spectra were recorded at room temperature on a Renishaw inVia Raman system and the laser line at 785 nm was used as an excitation source. Transmission electron microscopy (TEM) images were obtained by using a FEI Tecnai G2 F20 instrument operated at an accelerating voltage of 200 kV. Field emission scanning electron microscopy (FE-SEM) images were gained from a FEI Nova NanoSEM 230 instrument. UV-vis diffuse reflectance spectra (DRS) were collected by a Varian Cary 500 Scan UV-vis-NIR spectrometer with  $\text{BaSO}_4$  as the background. The Brunauer-Emmett-Teller (BET) specific surface area and porosities of the samples were measured on a Micromeritics ASAP2020 analyzer by  $\text{N}_2$  adsorption at 77 K. X-ray photoelectron spectroscopy (XPS) analysis was collected on a ESCALAB 250 photoelectron spectrometer (Thermo Fisher Scientific) with monochromatic Al  $\text{K}\alpha$  radiation ( $E = 1486.2$  eV). The photoelectrochemical data was collected by a CHI-660D electrochemical workstation (CH Instruments, USA). The photoelectrochemical experiment was carried out in a conventional three-electrode cell with a quartz window. The sample was deposited on a sheet of indium-tin-oxide (ITO) glass to serve as the working electrode with  $0.5\text{ cm} \times 0.5\text{ cm}$  area. A platinum wire and an Ag/AgCl electrode were used as the counter and reference electrodes, respectively. The electrolyte was 0.1 M  $\text{Na}_2\text{SO}_4$  solution. The detection of activated species was conducted by the spin-trapping electron spin resonance (ESR) measurement on a Bruker model A300 spectrometer. The settings were as follows: center field, 3512 G; microwave frequency, 9.86 GHz; microwave power, 20 mW.

### 2.3. Tests of photocatalytic activity

The photocatalytic degradation of methyl orange (MO) or Rhodamine B (RhB) as model reactions [39–43] was carried out in an aqueous solution at ambient temperature controlled by an air-cooling system. The light source was a 500 W Xe-arc lamp (Institute of Electric Light Source, Beijing). The 420 and 800 nm cutoff filters were placed in front of the vessel to ensure that the reactor was irradiated only by visible light ranging from 420 nm to 800 nm. When only 800 nm cutoff filter was used, the simulated solar light ranging from 320 nm to 800 nm was obtained. The transmission spectra of 420 and 800 nm combined cutoff filters, 800 nm cutoff filters and the 100 mL-Pyrex glass vessel were shown in Fig. S1 (in Supplementary data). A total of 0.08 g of photocatalyst was added to 80 mL of simulating pollutant solution, such as MO solution ( $1 \times 10^{-5}$  g/L, 10 ppm) or RhB solution ( $1 \times 10^{-5}$  mol/L, 10 ppm), contained in a 100 mL Pyrex glass vessel with a plane side. Before

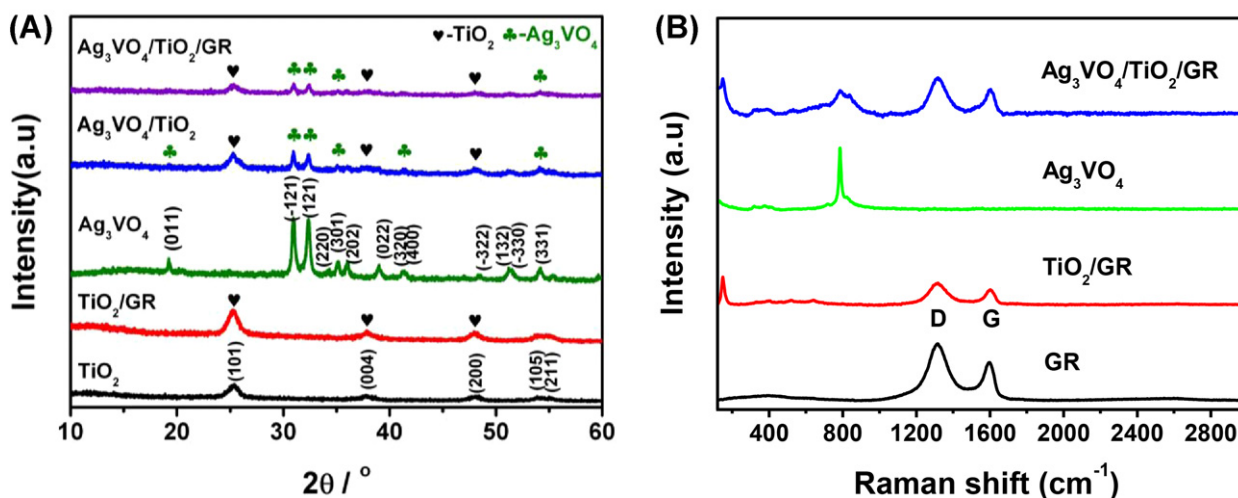


Fig. 1. (A) XRD patterns (the heart and club shape were used to stand for anatase  $\text{TiO}_2$  and  $\text{Ag}_3\text{VO}_4$  in the figure) and (B) Raman spectra of the synthesized samples.

irradiation, the suspension was magnetically stirred for 1 h in the dark in order to reach adsorption–desorption equilibrium between the catalyst and the simulating pollutant. 3 mL aliquots were sampled and centrifuged to remove the catalyst at given time intervals. Then the supernatants were analyzed to study the photocatalytic degradation of the target pollutants by using Varian Cary 50 UV-vis spectrophotometer.

### 3. Results and discussion

#### 3.1. Physicochemical properties of $\text{Ag}_3\text{VO}_4/\text{TiO}_2/\text{GR}$

##### 3.1.1. Component and structure

XRD patterns providing information on the crystalline nature of a series of samples were presented in Fig. 1A. The XRD pattern of  $\text{TiO}_2/\text{GR}$  nanocomposite was similar to that of as-prepared pure  $\text{TiO}_2$  as the comparison which completely corresponded to anatase crystalline phase  $\text{TiO}_2$  (JCPDS 21-1272). The synthesized  $\text{Ag}_3\text{VO}_4$  as the comparison was in accord with monoclinic  $\alpha\text{-Ag}_3\text{VO}_4$  (JCPDS 43-0542). The characteristic diffraction peaks of monoclinic  $\alpha\text{-Ag}_3\text{VO}_4$  and anatase  $\text{TiO}_2$  were obviously present in the XRD pattern of  $\text{Ag}_3\text{VO}_4/\text{TiO}_2/\text{GR}$  which is similar to that of  $\text{Ag}_3\text{VO}_4/\text{TiO}_2$ . Notably, no typical diffraction peaks belonging to the separate graphene (GR) were observed in the  $\text{TiO}_2/\text{GR}$  and  $\text{Ag}_3\text{VO}_4/\text{TiO}_2/\text{GR}$  nanocomposites. It has been previously reported that GO could be hydrothermally reduced to graphene in ethanol in a sealed autoclave [38]. Then, the absence of such peak corresponding to GR can be ascribed to the fact that the main characteristic peak of GR might be shielded by the main peak of anatase  $\text{TiO}_2$  [44]. Raman spectroscopic measurement was conducted to further elucidate the components of  $\text{Ag}_3\text{VO}_4/\text{TiO}_2/\text{GR}$  nanocomposite. As indicated in Fig. 1B, the peaks located at  $145\text{ cm}^{-1}$  and  $787\text{ cm}^{-1}$  present in Raman spectrum of  $\text{Ag}_3\text{VO}_4/\text{TiO}_2/\text{GR}$  corresponded to the main peaks of  $\text{TiO}_2$  (Fig. S2) and  $\text{Ag}_3\text{VO}_4$ , respectively. The other two peaks appearing in Raman spectrum of  $\text{Ag}_3\text{VO}_4/\text{TiO}_2/\text{GR}$  belonged to D band and G band of GR. The D band is due to the breathing modes of  $\text{sp}^2$  atoms in rings and is related to the occurrence of defects and structural disorder in graphene sheets. The G band is derived from the stretching of the  $\text{sp}^2$ -hybridized carbon–carbon bonds and is highly sensitive to strain effects in  $\text{sp}^2$  system within graphene sheets [35]. The analysis of Raman spectra combined with the results of XRD further confirmed the presence of three components in  $\text{Ag}_3\text{VO}_4/\text{TiO}_2/\text{GR}$  nanocomposite.

The morphology of prepared  $\text{TiO}_2/\text{GR}$ ,  $\text{Ag}_3\text{VO}_4/\text{TiO}_2$  and  $\text{Ag}_3\text{VO}_4/\text{TiO}_2/\text{GR}$  was observed with SEM (Fig. S3). The SEM image

of  $\text{Ag}_3\text{VO}_4/\text{TiO}_2$  composite (Fig. S3C) showed that there was no sheet-like structure when GR was absent. However, it was easy to observe many crumpled platelets decorated with nanoparticles in  $\text{TiO}_2/\text{GR}$  (Fig. S3A and B) and  $\text{Ag}_3\text{VO}_4/\text{TiO}_2/\text{GR}$  composite (Fig. S3D–F). Especially Fig. S3F showed a sheet of graphene with typical wrinkles and attached particles. It was believed that the observed crumpled sheets in Fig. S3 were graphene sheets.  $\text{TiO}_2$  and  $\text{Ag}_3\text{VO}_4$  both densely deposited on surface and the edge of the corrugated graphene sheets in  $\text{Ag}_3\text{VO}_4/\text{TiO}_2/\text{GR}$  composite (Fig. S3D–F) and the morphology changed little compared with  $\text{TiO}_2/\text{GR}$  (Fig. S3A and B). The sizes of the composite sheets were in micrometer scale both in length and width, which allows an easy separation from the reaction system by conventional filtration. The formation and structure of  $\text{Ag}_3\text{VO}_4/\text{TiO}_2/\text{GR}$  nanocomposite was further confirmed by TEM analysis, and the representative images were shown in Fig. 2. The obvious edges and crumpled silk waves of these graphene sheets (the locations which the arrows pointed at) shown in Fig. 2A and C led us to believe that these nanoparticles were indeed deposited on the almost transparent graphene sheets as the support. As shown in Fig. 2A,  $\text{TiO}_2$  nanoparticles were uniformly dispersed on graphene sheets by hydrothermal treatment. By further processing,  $\text{Ag}_3\text{VO}_4$  and  $\text{TiO}_2$  with different sizes and contrasts were both deposited on graphene sheets (Fig. 2C). Compared with  $\text{Ag}_3\text{VO}_4/\text{TiO}_2$  nanocomposite (Fig. 2B), the nanoparticles in  $\text{Ag}_3\text{VO}_4/\text{TiO}_2/\text{GR}$  nanocomposite possessed better dispersion degree. The high resolution transmission electron microscopy (HRTEM) image of  $\text{Ag}_3\text{VO}_4/\text{TiO}_2/\text{GR}$  (the marked location of Fig. 2C with one black circle) was presented in Fig. 2D. The fringes of  $d = 0.25\text{ nm}$ ,  $d = 0.22\text{ nm}$  and  $d = 0.23\text{ nm}$  observed in Fig. 2D matched those of (301) and (400) and (022) crystallographic planes of  $\text{Ag}_3\text{VO}_4$ . The fringes of  $d = 0.35\text{ nm}$  and  $d = 0.19\text{ nm}$  corresponded to the (101) and (200) crystallographic planes of anatase  $\text{TiO}_2$ . The intimate contact took place between the coupling  $\text{Ag}_3\text{VO}_4$  and  $\text{TiO}_2$  in  $\text{Ag}_3\text{VO}_4/\text{TiO}_2/\text{GR}$  nanocomposite.

##### 3.1.2. Wide spectral response

As is known to all, the wavelength range of light absorption for photocatalyst plays an important role in the photocatalysis, especially for the visible light photocatalytic degradation of organic pollutants. The UV-vis DRS patterns of  $\text{TiO}_2$ ,  $\text{Ag}_3\text{VO}_4$ ,  $\text{TiO}_2/\text{GR}$ ,  $\text{Ag}_3\text{VO}_4/\text{TiO}_2$  and  $\text{Ag}_3\text{VO}_4/\text{TiO}_2/\text{GR}$  composites were shown in Fig. 3. The values of band gap for  $\text{Ag}_3\text{VO}_4$  and  $\text{TiO}_2$  estimated by the onset point of the absorption curve was 2.2 eV and 3.2 eV, respectively. The result of  $\text{Ag}_3\text{VO}_4$  was in agreement with that reported by Konta et al. [36]. Based on the analysis of DRS, there was an



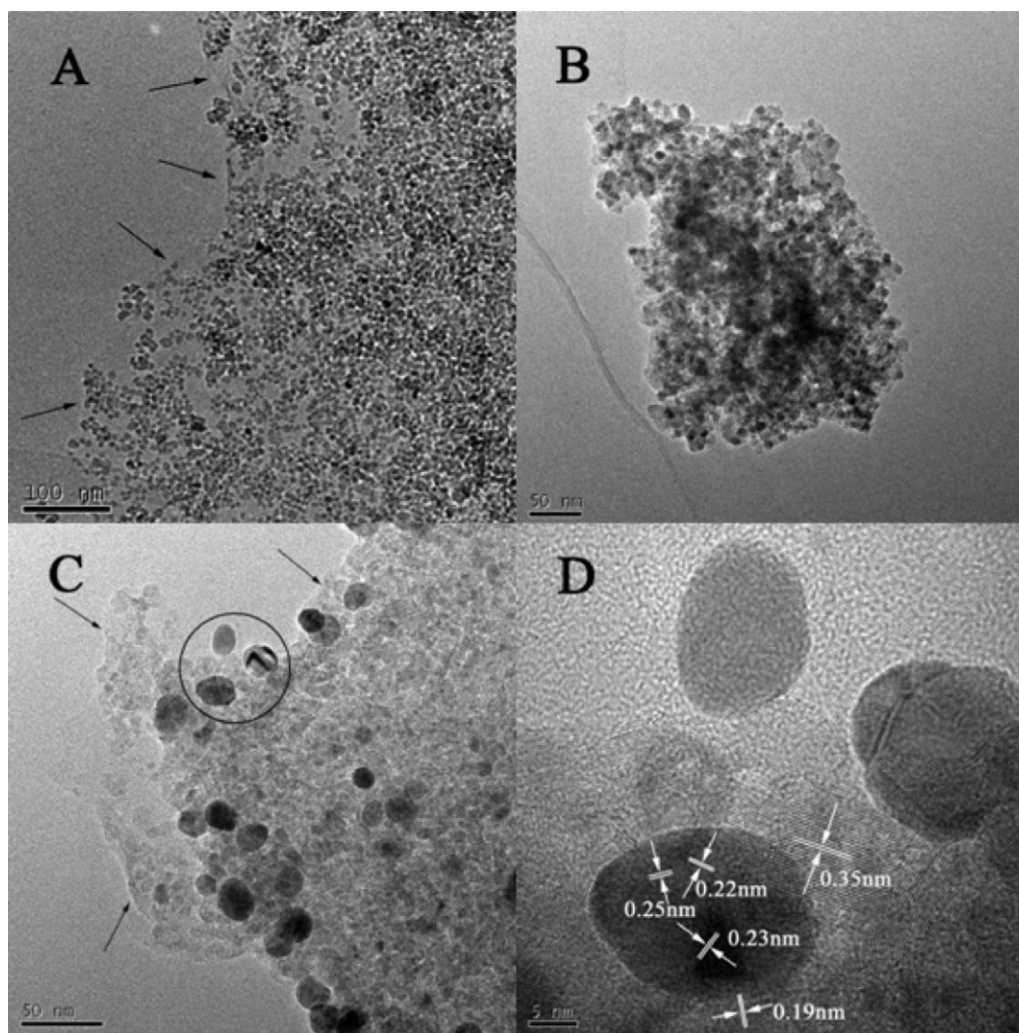


**Fig. 2.** TEM images of (A)  $\text{TiO}_2/\text{GR}$ , (B)  $\text{Ag}_3\text{VO}_4/\text{TiO}_2$ , (C)  $\text{Ag}_3\text{VO}_4/\text{TiO}_2/\text{GR}$  and (D) HRTEM image of  $\text{Ag}_3\text{VO}_4/\text{TiO}_2/\text{GR}$  (image D is the amplification of the marked location of image C with one black circle).

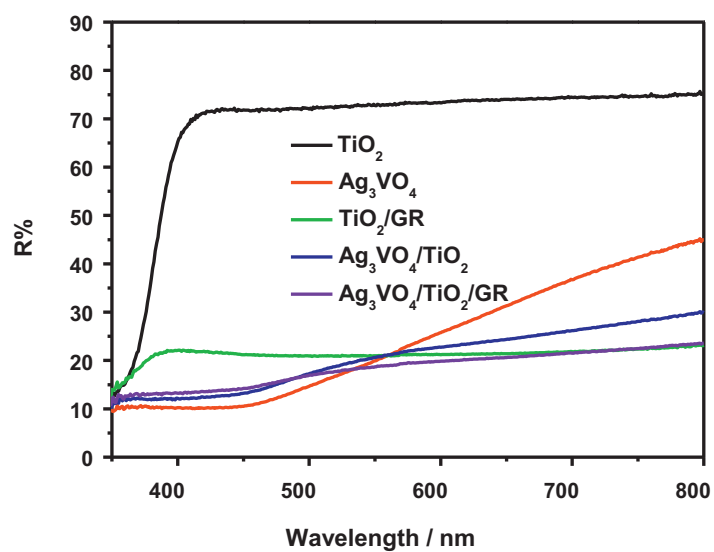


**Fig. 3.** UV-vis DRS patterns of the prepared samples.

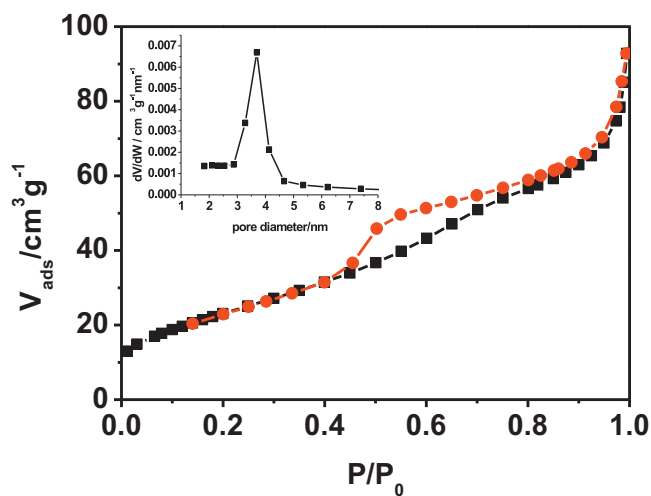


Fig. 4. Nitrogen adsorption-desorption isotherm and pore size distribution plot (inset) of the as-prepared  $\text{Ag}_3\text{VO}_4/\text{TiO}_2/\text{GR}$ .

obvious enhancement in the visible light absorption of  $\text{TiO}_2/\text{GR}$  powder, compared to bare  $\text{TiO}_2$ . Moreover, the light absorption range of  $\text{Ag}_3\text{VO}_4/\text{TiO}_2/\text{GR}$  was further extended with the introduction of  $\text{Ag}_3\text{VO}_4$  and then the  $\text{Ag}_3\text{VO}_4/\text{TiO}_2/\text{GR}$  composite possessed wide spectral response including UV and visible light wavelength. So, a more efficient utilization of the solar spectrum on  $\text{Ag}_3\text{VO}_4/\text{TiO}_2/\text{GR}$  could be achieved, which contributed to the improvement in its photocatalytic activity and facilitated its use in practical environmental remediation.

### 3.1.3. BET analysis

The nitrogen adsorption-desorption isotherm and pore size distribution plot (inset) of the as-prepared  $\text{Ag}_3\text{VO}_4/\text{TiO}_2/\text{GR}$  sample were presented in Fig. 4. The BET specific surface area of  $\text{Ag}_3\text{VO}_4/\text{TiO}_2/\text{GR}$  was determined to be  $86 \text{ m}^2 \text{ g}^{-1}$ .  $\text{N}_2$ -sorption isotherm of the  $\text{Ag}_3\text{VO}_4/\text{TiO}_2/\text{GR}$  sample belonged to type-IV isotherm with a hysteresis loop according to BDDT (Brunauer, Deming, Deming and Teller) classification, which was typical characterization of mesoporous materials [45–47]. The Barrett-Joyner-Halenda (BJH) pore size distribution of  $\text{Ag}_3\text{VO}_4/\text{TiO}_2/\text{GR}$  composite was narrow, and the most probable pore diameter was 3.5 nm which was in the mesoporous region [45]. The above results indicated that  $\text{Ag}_3\text{VO}_4/\text{TiO}_2/\text{GR}$  composite was a porous material.

### 3.2. Photocatalytic activity and stability

The photocatalytic activities for liquid-phase degradation of MO over the prepared photocatalysts under visible light and simulated solar light irradiation have been tested at room temperature. Commercial Degussa P25 and nitrogen-doped  $\text{TiO}_2$  ( $\text{TiO}_{2-x}\text{N}_x$ ) were employed as comparison.  $\text{TiO}_{2-x}\text{N}_x$  was obtained by traditional process with calcining  $\text{TiO}_2$  xerogel at  $550^\circ\text{C}$  under dry  $\text{NH}_3$  flow for 3 h [48]. As seen from Fig. 5A, after 3 h of visible light irradiation ( $420 \text{ nm} < \lambda < 800 \text{ nm}$ ), the photocatalytic conversion ratios of MO for  $\text{TiO}_2/\text{GR}$ ,  $\text{TiO}_{2-x}\text{N}_x$ , P25,  $\text{Ag}_3\text{VO}_4/\text{TiO}_2$ ,  $\text{Ag}_3\text{VO}_4$ ,  $\text{Ag}_3\text{VO}_4/\text{TiO}_2/\text{GR}$  were 6%, 11%, 13%, 38%, 66%, 81%, respectively.  $\text{Ag}_3\text{VO}_4/\text{TiO}_2/\text{GR}$  composite performed the optimal visible photocatalytic activity in degradation of MO among them.  $\text{Ag}_3\text{VO}_4/\text{TiO}_2$  nanocomposite prepared by wet chemical method exhibited lower photocatalytic activity than  $\text{Ag}_3\text{VO}_4$  due to the low efficiency of these heterojunctions between  $\text{Ag}_3\text{VO}_4$  and  $\text{TiO}_2$  resulting in inefficient electron transfer process of activated  $\text{Ag}_3\text{VO}_4$  to  $\text{TiO}_2$ .  $\text{Ag}_3\text{VO}_4/\text{TiO}_2/\text{GR}$  performed higher visible photocatalytic activity than  $\text{Ag}_3\text{VO}_4/\text{TiO}_2$ ,

which demonstrated the introduction of GR contributed to the enhancement of activity. As shown in Fig. S4,  $\text{Ag}_3\text{VO}_4/\text{TiO}_2/\text{GR}$  still maintained the superiority in activity under simulated solar light irradiation ( $320 \text{ nm} < \lambda < 800 \text{ nm}$ ).

Blank experiment of RhB without any photocatalyst, labeled by blank, showed that no activity was observed under simulated solar light irradiation.  $\text{TiO}_2$  and  $\text{TiO}_{2-x}\text{N}_x$  showed little photocatalytic activity, far lower than  $\text{Ag}_3\text{VO}_4/\text{TiO}_2/\text{GR}$  within the same interval.  $\text{Ag}_3\text{VO}_4/\text{TiO}_2/\text{GR}$  nearly completely degraded 10 ppm RhB within 40 min under visible light irradiation or within 25 min under simulated solar light irradiation. As displayed in Fig. 5B, the photocatalytic degradation process of RhB is fit for pseudo first-order kinetics by linear transform  $\ln(C_0/C_t) = kt$  [49]. The apparent rate constant  $k$  corresponding to P25,  $\text{Ag}_3\text{VO}_4/\text{TiO}_2$  and  $\text{Ag}_3\text{VO}_4/\text{TiO}_2/\text{GR}$  are  $0.017 \text{ min}^{-1}$ ,  $0.044 \text{ min}^{-1}$ ,  $0.065 \text{ min}^{-1}$  under visible light and  $0.097 \text{ min}^{-1}$ ,  $0.073 \text{ min}^{-1}$ ,  $0.111 \text{ min}^{-1}$  under simulated solar light irradiation, respectively.  $\text{Ag}_3\text{VO}_4/\text{TiO}_2/\text{GR}$  composite possessed the optimal photocatalytic activity in degradation of RhB among them whether in visible or simulated solar light irradiation. The apparent rate constant  $k$  of  $\text{Ag}_3\text{VO}_4/\text{TiO}_2/\text{GR}$  under simulated solar light was nearly two times higher than that under visible light, which further confirmed the wide spectral response and the effective utilization of solar energy for  $\text{Ag}_3\text{VO}_4/\text{TiO}_2/\text{GR}$  photocatalyst.

Besides MO and RhB, p-chlorophenol (p-CP) as a kind of difficult degradable colorless organic pollutant was used to evaluate the photocatalytic activity of the prepared  $\text{Ag}_3\text{VO}_4/\text{TiO}_2/\text{GR}$  photocatalyst under visible light irradiation. Its degradation can exclude the photosensitized reaction.  $\text{Ag}_3\text{VO}_4/\text{TiO}_2/\text{GR}$  photocatalyst nearly degraded 10 ppm p-CP by 30% after 5 h of visible light irradiation, which further indicated that  $\text{Ag}_3\text{VO}_4/\text{TiO}_2/\text{GR}$  composite possessed high visible photocatalytic activity (Fig. S5).

Moreover, the stability of our  $\text{Ag}_3\text{VO}_4/\text{TiO}_2/\text{GR}$  nanocomposite was evaluated repeatedly four times in terms of performing the RhB degradation under simulated solar light irradiation (shown in Fig. 6A). The photocatalytic efficiency displayed slight decrease after the reaction was performed consecutive four times. On the basis of XPS analysis of used sample and fresh sample (Fig. 6B), the chemical state of photocatalyst did not change after the photocatalytic reaction. Therefore, it is believed that  $\text{Ag}_3\text{VO}_4/\text{TiO}_2/\text{GR}$  nanocomposite possessed activity stability which was crucial to assess a photocatalyst and its application.

### 3.3. Discussion of photocatalytic mechanism

#### 3.3.1. Photoelectrochemical property

Photoelectrochemical measurement was performed to further investigate the enhancement mechanism for photocatalytic activity of  $\text{Ag}_3\text{VO}_4/\text{TiO}_2/\text{GR}$  composite by introducing GR as the support. The transient photocurrent response has been demonstrated to be a useful technique for investigating the efficiency of the separation of photogenerated electron-hole pairs [50]. Fig. 7 represented the photocurrent versus time curves for the samples with several on-off cycles of intermittent visible and simulated solar light irradiation. For the same sample, its photocurrent under simulated solar light irradiation was higher than that under visible light irradiation. The  $\text{Ag}_3\text{VO}_4/\text{TiO}_2/\text{GR}$  composite exhibited a significantly higher photocurrent than  $\text{Ag}_3\text{VO}_4/\text{TiO}_2$  composite, and  $\text{TiO}_2/\text{GR}$  possessed the lowest photocurrent among them. The photocurrent of  $\text{Ag}_3\text{VO}_4/\text{TiO}_2/\text{GR}$  was obviously larger than the addition of the photocurrents of  $\text{Ag}_3\text{VO}_4/\text{TiO}_2$  and  $\text{TiO}_2/\text{GR}$ , which further confirmed that the interaction existed in  $\text{Ag}_3\text{VO}_4/\text{TiO}_2/\text{GR}$  composite rather than simple mixture. It's important to note that the shapes of photocurrent curves of  $\text{Ag}_3\text{VO}_4/\text{TiO}_2/\text{GR}$  and  $\text{Ag}_3\text{VO}_4/\text{TiO}_2$  had a great difference. When  $\text{Ag}_3\text{VO}_4/\text{TiO}_2$  electrode was illuminated, its photocurrent curve (Fig. 7C and D) initially presented a spike

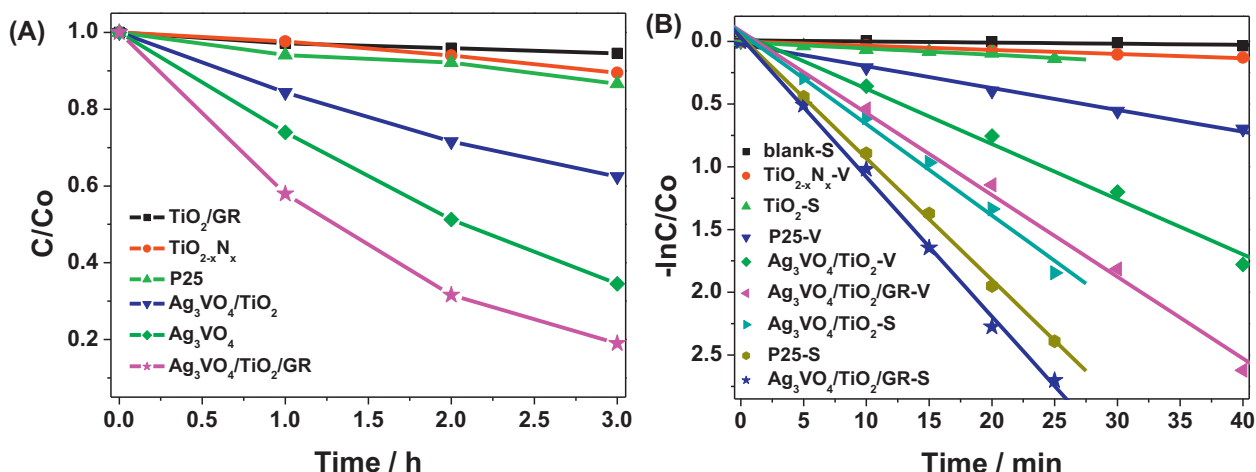


**Fig. 5.** (A) Liquid-phase photocatalytic degradation of 10 ppm MO under visible light and (B) kinetic linear simulation curves of 10 ppm RhB over the prepared photocatalysts,  $\text{TiO}_{2-x}\text{N}_x$  and P25 (V and S following the sample name in Fig. 5B respectively represented the visible light and simulated solar light irradiation).

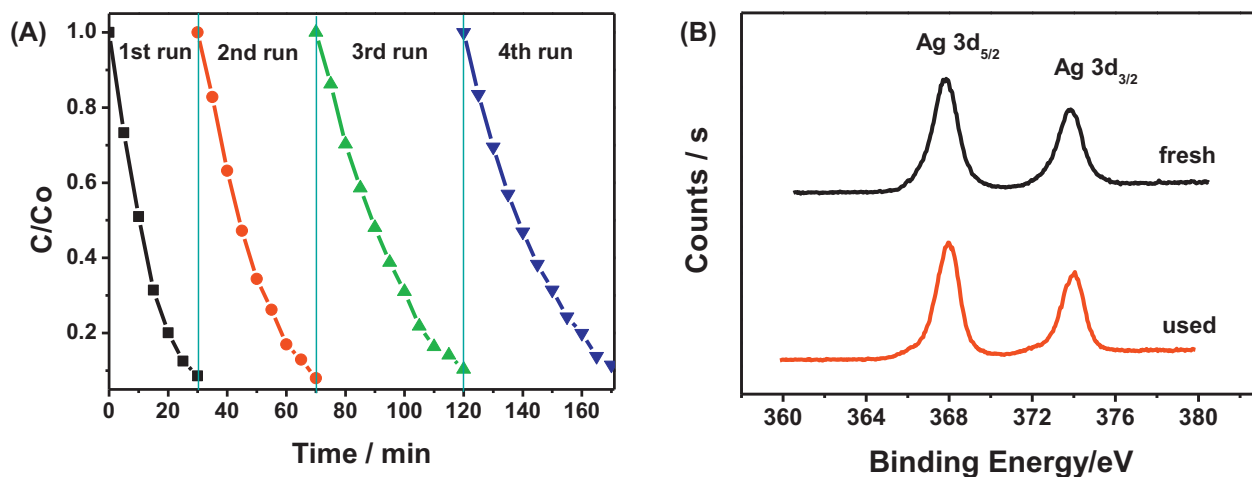


**Fig. 6.** (A) Photocatalytic degradation stability of RhB over  $\text{Ag}_3\text{VO}_4/\text{TiO}_2/\text{GR}$  nanocomposite and (b) comparison of Ag 3d XPS spectra between used and fresh sample under simulated solar light irradiation ( $320 \text{ nm} < \lambda < 800 \text{ nm}$ ).

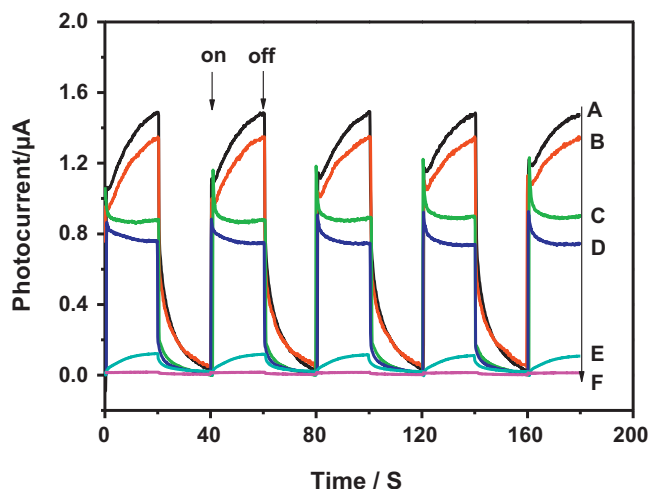


**Fig. 7.** Transient photocurrent responses versus time for (A)  $\text{Ag}_3\text{VO}_4/\text{TiO}_2/\text{GR}$ , (C)  $\text{Ag}_3\text{VO}_4/\text{TiO}_2$ , (E)  $\text{TiO}_2/\text{GR}$  under simulated solar light irradiation and (B)  $\text{Ag}_3\text{VO}_4/\text{TiO}_2/\text{GR}$ , (D)  $\text{Ag}_3\text{VO}_4/\text{TiO}_2$ , (F)  $\text{TiO}_2/\text{GR}$  under visible light irradiation.

and then the spike gradually decays until the photocurrent reached a stable value. The decrease in the photocurrent indicates that recombination is occurring within the  $\text{Ag}_3\text{VO}_4/\text{TiO}_2$  electrode [51]. Although the photogenerated electrons on the conduction band of  $\text{Ag}_3\text{VO}_4$  can transfer to  $\text{TiO}_2$ , the electrons left in  $\text{Ag}_3\text{VO}_4$  were easy to recombine with holes [52,53]. For  $\text{Ag}_3\text{VO}_4/\text{TiO}_2/\text{GR}$  electrode, its photocurrent (Fig. 7A and B) gradually increased under light illumination. After the illumination was turned off the photocurrent did not suddenly disappear but slowly decreased. After the introduction of GR into  $\text{Ag}_3\text{VO}_4/\text{TiO}_2$ , its decay of photocurrent in the initial seconds of illumination was eliminated. The reason was that some photogenerated electrons of  $\text{Ag}_3\text{VO}_4$  which did not directly transfer to  $\text{TiO}_2$ , transferred to GR and were stored within GR. So the recombination of photogenerated electrons and holes was inhibited to some degree. The photocurrent was generated from electrons on the conduction band of  $\text{TiO}_2$  transferred from GR sheets rather than  $\text{Ag}_3\text{VO}_4$  directly, resulting in the gradual increase in photocurrent. When the light was switched off, the gradual release of electrons from GR sheets with the electron storage effect led to the gradual decrease of photocurrent. The observed enhancement in the photocurrent intensity and the difference in shapes of photocurrent curves between  $\text{Ag}_3\text{VO}_4/\text{TiO}_2/\text{GR}$  and  $\text{Ag}_3\text{VO}_4/\text{TiO}_2$  demonstrated the increase in the efficiency of the separation of photogenerated

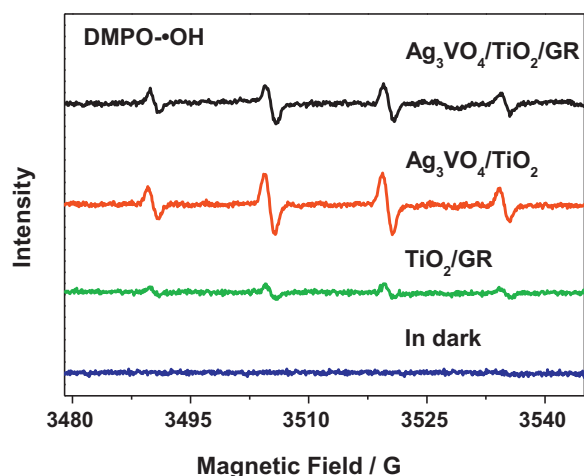


Fig. 8. DMPO spin-trapping ESR spectra on  $\text{Ag}_3\text{VO}_4/\text{TiO}_2/\text{GR}$  in aqueous dispersion for  $\text{DMPO}\cdot\text{OH}$  under simulated solar light irradiation.

electron–hole pairs and further confirmed the ability of GR to capture and shuttle electrons through the  $\pi$ – $\pi$  network [46,50,54].

Electrochemical impedance spectroscopy (EIS) was also used to investigate the effect of GR on the separation efficiency of photo-generated charges on  $\text{Ag}_3\text{VO}_4/\text{TiO}_2/\text{GR}$ ,  $\text{Ag}_3\text{VO}_4/\text{TiO}_2$  and  $\text{TiO}_2/\text{GR}$  under visible light and simulated solar light irradiation (Fig. S6). The radius of the arc on the EIS Nyquist plot represents the charge transfer step occurring at the surface of the electrode [55]. The results of EIS plot demonstrated that the efficiency of the separation of photogenerated electron–hole pairs increased in the order of  $\text{TiO}_2/\text{GR} < \text{Ag}_3\text{VO}_4/\text{TiO}_2 < \text{Ag}_3\text{VO}_4/\text{TiO}_2/\text{GR}$ . The results were in good agreement with the photocurrent measurements. This means that the interfacial charges can transfer more rapidly and induce effective separation of photoinduced electron–hole charge pairs.

### 3.3.2. Detection of active species

The presence of graphene in the  $\text{Ag}_3\text{VO}_4/\text{TiO}_2/\text{GR}$  nanocomposite can effectively inhibit the electron–hole pair recombination, which may caused more radical species with strong oxidation capability, such as hydroxyl radical ( $\cdot\text{OH}$ ) and superoxide radical ( $\text{O}_2^{\cdot-}$ ) species, for the degradation of pollutant. In order to further confirm that, ESR spin-trapping technique with 5,5-Dimethyl-1-pyrroline-N-oxide (DMPO) was carried out to detect the active species under simulated solar light irradiation ( $320\text{ nm} < \lambda < 800\text{ nm}$ ). Surprisingly, the intensity of  $\text{Ag}_3\text{VO}_4/\text{TiO}_2/\text{GR}$  for  $\text{DMPO}\cdot\text{OH}$  is lower than  $\text{Ag}_3\text{VO}_4/\text{TiO}_2$  (shown in Fig. 8). The reason was discussed in the latter photocatalytic mechanism section.  $\text{DMPO}\cdot\text{O}_2^{\cdot-}$  was not detected for  $\text{Ag}_3\text{VO}_4/\text{TiO}_2/\text{GR}$  system. There may be two reasons for the phenomenon. First, electrons can become trapped and reduce dioxygen to superoxide  $\text{O}_2^{\cdot-}$  or to hydrogen peroxide  $\text{H}_2\text{O}_2$  [1]. There is competition between two pathways. Second,  $\text{O}_2^{\cdot-}$  may react with  $\text{H}_2\text{O}_2$  to form  $\cdot\text{OH}$  radical [56]. So, the amount of  $\text{O}_2^{\cdot-}$  decreased too fast to be detected. The N,N-diethyl-p-phenylenediamine (DPD) method was widely employed for the detection of  $\text{H}_2\text{O}_2$ . This method is based on the horseradish peroxidase (POD)-catalyzed oxidation by  $\text{H}_2\text{O}_2$  of DPD [57]. The sequence of reaction led to the formation of the radical cation  $\text{DPD}^{\cdot+}$ , which formed a fairly stable color, with the absorption maxima at 510 nm and one at 551 nm. The result was shown in Fig. 9. For the water sample, there was no obvious absorption peak observed under the same condition. Apparently, the amount of  $\text{H}_2\text{O}_2$  followed the order  $\text{Ag}_3\text{VO}_4/\text{TiO}_2/\text{GR} > \text{Ag}_3\text{VO}_4 > \text{Ag}_3\text{VO}_4/\text{TiO}_2 > \text{TiO}_2/\text{GR}$ , which was in accord with the order of their photocatalytic activities. The results

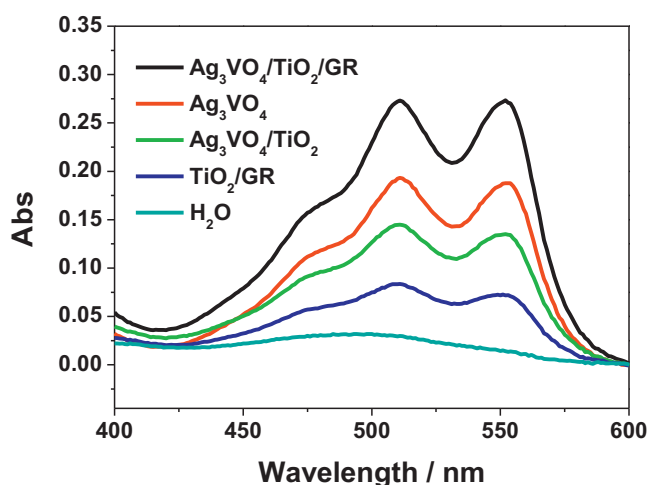


Fig. 9. Absorption spectra of the DPD/POD reagent after reaction with different samples under 0.5 h of simulated solar light irradiation.

of  $\text{H}_2\text{O}_2$  detection further demonstrated the probable eventual destination of electrons.

To further investigate the roles of these active species such as electrons/holes,  $\cdot\text{OH}$  and  $\text{O}_2^{\cdot-}$  in photocatalytic degradation process, different types of active species scavengers were added in catalyst system. Fig. 10 showed the photocatalytic activity of  $\text{Ag}_3\text{VO}_4/\text{TiO}_2/\text{GR}$  nanocomposite toward the degradation of RhB under the different conditions. After 0.1 g of ammonium oxalate (AO) as a hole-scavenger was added into the reaction system [58], the decrease in the rate of degradation of RhB over  $\text{Ag}_3\text{VO}_4/\text{TiO}_2/\text{GR}$  was the most obvious, which meant the photogenerated holes may play an important role in the photocatalytic degradation. The benzoquinone (BQ) has the ability to trap  $\text{O}_2^{\cdot-}$  by a simple electron transfer mechanism [59]. The addition of BQ (1 mg) provoked partial inhibition of the RhB degradation.  $\text{N}_2$  was bubbled through the suspension at the rate of 20 mL/min to ensure that the reaction was operated without dissolved  $\text{O}_2$  as an electron scavenger to produce a variety of active oxygen species. The following decrease of activity further indicated  $\text{O}_2^{\cdot-}$  played a role in the degradation of RhB. After 2 mL of tert-butyl alcohol (TBA) as a scavenger for  $\cdot\text{OH}$  was added in the system, it did not obviously impact the decomposition rate. So, the degradation of RhB was driven by the contribution of

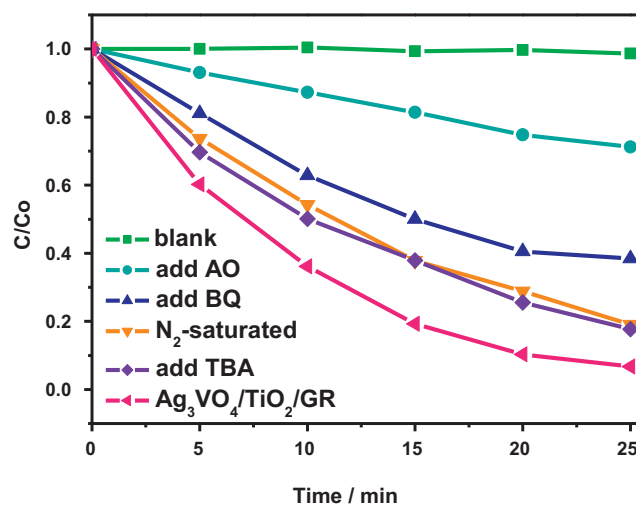
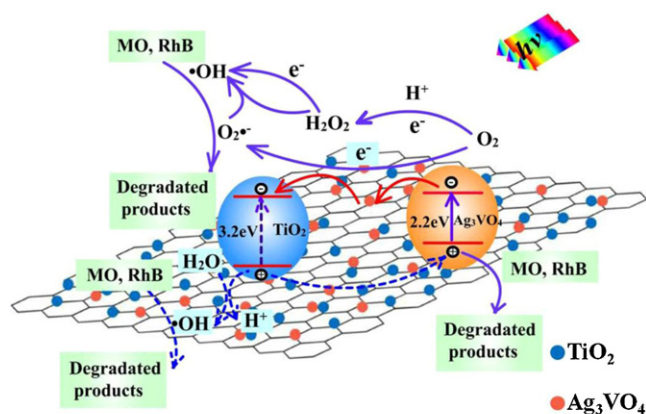


Fig. 10. Photocatalytic degradation of RhB over  $\text{Ag}_3\text{VO}_4/\text{TiO}_2/\text{GR}$  nanocomposite under different conditions with exposure to simulated solar light ( $320\text{ nm} < \lambda < 800\text{ nm}$ ).





**Scheme 1.** Proposed mechanism for photocatalytic degradation of organic pollutants (MO, RhB) on  $\text{Ag}_3\text{VO}_4/\text{TiO}_2/\text{GR}$  nanocomposite (black sheet represented GR in the diagram) under visible light irradiation (solid line) and simulated solar light irradiation (solid line and dashed line).

$\bullet\text{OH}$  radicals to a lesser extent. Based on the integrated analysis of these results, we can conclude that the degradation of RhB was driven mainly by the participation of holes and  $\text{O}_2^{\bullet-}$  radicals played a secondary role and  $\bullet\text{OH}$  radicals to a lesser extent partook in that process.

### 3.3.3. The proposed photocatalytic mechanism

The relative positions of energy bands of  $\text{Ag}_3\text{VO}_4$  and  $\text{TiO}_2$  were known according to the results reported in the literature [53]. Based on the results of photoelectrochemical measurement, ESR spin-trapping technique, DPD method and the addition of active species scavengers, the mechanism for photocatalytic degradation of organic pollutants (MO, RhB) on  $\text{Ag}_3\text{VO}_4/\text{TiO}_2/\text{GR}$  nanocomposite was proposed and represented in Scheme 1. For  $\text{Ag}_3\text{VO}_4/\text{TiO}_2/\text{GR}$  nanocomposite,  $\text{Ag}_3\text{VO}_4$  and  $\text{TiO}_2$  dispersed on the GR sheet. Some  $\text{Ag}_3\text{VO}_4$  and  $\text{TiO}_2$  particles contacted intimately and some separated. For close contacting  $\text{Ag}_3\text{VO}_4$  and  $\text{TiO}_2$  under simulated solar light irradiation, the excited electrons on conduction band (CB) of  $\text{Ag}_3\text{VO}_4$  can directly transfer to CB of  $\text{TiO}_2$ , and the excited holes on valence band (VB) of  $\text{TiO}_2$  also can directly transfer to VB of  $\text{Ag}_3\text{VO}_4$ , which did not happen under visible light irradiation. For separated  $\text{Ag}_3\text{VO}_4$  and  $\text{TiO}_2$ , the pathways of electron transfer between them changed. When subjected to simulated solar light irradiation, the photogenerated electrons transferred from CB of  $\text{Ag}_3\text{VO}_4$  to the graphene sheets. The two-dimensional planar conjugation structure in graphene facilitated interfacial charge transfer along the graphene sheets to  $\text{TiO}_2$  and subsequently an effective charge separation was achieved. Then, electrons were trapped by the adsorbed molecular oxygen on the  $\text{TiO}_2$  surface to produce superoxide anion ( $\text{O}_2^{\bullet-}$ ) radicals or  $\text{H}_2\text{O}_2$  [1]. Electrons left on  $\text{Ag}_3\text{VO}_4$  also could be trapped to form  $\text{O}_2^{\bullet-}$  radicals or  $\text{H}_2\text{O}_2$ . The production of  $\text{H}_2\text{O}_2$  in our photocatalytic system was confirmed by DPD method and the role of  $\text{O}_2^{\bullet-}$  was confirmed by method of active species scavengers. The transfer of holes from VB of  $\text{TiO}_2$  to  $\text{Ag}_3\text{VO}_4$  was accelerated with the addition of GR, which was demonstrated by the decrease in intensity of  $\bullet\text{OH}$  for  $\text{Ag}_3\text{VO}_4/\text{TiO}_2/\text{GR}$  compared with  $\text{Ag}_3\text{VO}_4/\text{TiO}_2$  detected by ESR technique. The photogenerated holes on VB of  $\text{TiO}_2$  can directly oxidate water to generate  $\bullet\text{OH}$  radical but the holes on  $\text{Ag}_3\text{VO}_4$  cannot oxidate water although they easily activated organic pollutants, leading to a subsequent decomposition. The holes indeed played an important role in  $\text{Ag}_3\text{VO}_4/\text{TiO}_2/\text{GR}$  photocatalytic system on the basis of the results of active species scavengers. As a result, the ability of GR to capture and shuttle electrons enhanced the efficiency of the separation of photogenerated electron–hole pairs so that they can be fully involved in the

photocatalytic reactions and a highly efficient photocatalytic activity was achieved.

## 4. Conclusions

$\text{Ag}_3\text{VO}_4/\text{TiO}_2/\text{graphene}$  nanocomposite prepared first by a two-step process possessed a wide spectral response and exhibited obviously increased photocatalytic activity in degradation of organic pollutants including methyl orange and Rhodamine B, compared with  $\text{Ag}_3\text{VO}_4/\text{TiO}_2$  and  $\text{TiO}_2/\text{GR}$  nanocomposites. The enhancement of photocatalytic activity was attributed to three aspects: first, light absorption was extended to longer wavelengths to reach wide spectral response; second, graphene as support material contributed to the uniform dispersion of  $\text{Ag}_3\text{VO}_4$  and  $\text{TiO}_2$  nanoparticles on graphene sheets; third, the formation of heterojunction between  $\text{Ag}_3\text{VO}_4$  and  $\text{TiO}_2$  and the capacity of storing and shuttling electrons of graphene inhibited the photogenerated carriers recombination. Based on the results of detection of active species, we can conclude that the degradation of RhB was driven mainly by the participation of holes,  $\text{O}_2^{\bullet-}$  radicals and  $\bullet\text{OH}$  radicals and  $\text{H}_2\text{O}_2$  to a lesser extent partook in this process. Therefore, the transfer of photogenerated carriers and photocatalytic degradation mechanism on  $\text{Ag}_3\text{VO}_4/\text{TiO}_2/\text{GR}$  nanocomposite were proposed and discussed.

## Acknowledgments

This work was financially supported by the National Natural Science Foundation of China (21173047, 21073036 and 21033003), and National Basic Research Program of China (973 Program, 2013CB632405).

## Appendix A. Supplementary data

Supplementary data associated with this article can be found, in the online version, at <http://dx.doi.org/10.1016/j.apcatb.2013.02.010>.

## References

- [1] A. Fujishima, T.N. Rao, D.A. Tryk, *Journal of Photochemistry and Photobiology C: Photochemistry Review* 1 (2000) 1–21.
- [2] G.D. Jiang, Z.F. Lin, C. Chen, L.H. Zhu, Q. Chang, N. Wang, W. Wei, H.Q. Tang, *Carbon* 49 (2011) 2693–2701.
- [3] T. Bak, J. Nowotny, M. Rekas, C.C. Sorrell, *International Journal of Hydrogen Energy* 27 (2002) 991–1022.
- [4] A. Kudo, Y. Miseki, *Chemical Society Reviews* 38 (2009) 253–278.
- [5] X. Yang, F.Y. Ma, K.X. Li, Y.N. Guo, J.L. Hu, W. Li, M.X. Huo, Y.H. Guo, *Journal of Hazardous Materials* 175 (2010) 429–438.
- [6] K. Chen, J.Y. Li, J. Li, Y.M. Zhang, W.X. Wang, *Colloids and Surfaces A: Physicochemical and Engineering Aspects* 360 (2010) 47–56.
- [7] L.G. Devi, B.N. Murthy, S.G. Kumar, *Journal of Molecular Catalysis A: Chemical* 308 (2009) 174–181.
- [8] D. Dvoranová, V. Brezová, M. Mazúr, M.A. Malati, *Applied Catalysis B: Environmental* 37 (2002) 91–105.
- [9] C.M. Teh, A.R. Mohamed, *Journal of Alloys and Compounds* 509 (2011) 1648–1660.
- [10] D. Chatterjee, A. Mahata, *Journal of Photochemistry and Photobiology A* 153 (2002) 199–204.
- [11] D. Chatterjee, S. Dasgupta, *Journal of Photochemistry and Photobiology C* 6 (2005) 186–205.
- [12] I. Nakamura, N. Negishi, S. Kutsuna, T. Ihara, S. Sugihara, K. Takeuchi, *Journal of Molecular Catalysis A: Chemical* 161 (2000) 205–212.
- [13] Y. Bessekhouad, D. Robert, J.V. Weber, *Journal of Photochemistry and Photobiology A* 163 (2004) 569–580.
- [14] Y. Bessekhouad, D. Robert, J.V. Weber, *Catalysis Today* 101 (2005) 315–321.
- [15] J.S. Jang, W. Li, S. Hyuk Oh, J.S. Lee, *Chemical Physics Letters* 425 (2006) 278–282.
- [16] H.M. Jia, H. Xu, Y. Hu, Y.W. Tang, L. z. Zhang, *Electrochemistry Communications* 9 (2007) 354–360.
- [17] B. Gao, Y.J. Kim, A.K. Chakraborty, W.I. Lee, *Applied Catalysis B: Environmental* 83 (2008) 202–207.
- [18] B.T. Jiang, S.Y. Zhang, X.z. Guo, B.K. Jin, Y.P. Tian, *Applied Surface Science* 255 (2009) 5975–5978.



- [19] Y. Hu, D.Z. Li, Y. Zheng, W. Chen, Y.H. He, Y. Shao, X.Z. Fu, G.C. Xiao, *Applied Catalysis B: Environmental* 104 (2011) 30–36.
- [20] H.J. Huang, D.Z. Li, Q. Lin, W.J. Zhang, Y. Shao, Y.B. Chen, M. Sun, X.Z. Fu, *Environmental Science and Technology* 43 (2009) 4164–4168.
- [21] G.C. Xiao, X.C. Wang, D.Z. Li, X.Z. Fu, *Journal of Photochemistry and Photobiology A* 193 (2008) 213–221.
- [22] J.H. Yan, L. Zhang, H.H. Yang, Y.G. Tang, Z.G. Lu, S.L. Guo, Y.L. Dai, Y. Han, M.H. Yao, *Solar Energy* 83 (2009) 1534–1539.
- [23] S. Rehman, R. Ullah, A.M. Butt, N.D. Gohar, *Journal of Hazardous Materials* 170 (2009) 560–569.
- [24] S.Y. Chai, Y.J. Kim, M.H. Jung, A.K. Chakraborty, D.W. Jung, W.I. Lee, *Journal of Catalysis* 262 (2009) 144–149.
- [25] X.P. Lin, J.C. Xing, W.D. Wang, Z.C. Shan, F.F. Xu, F.G. Huang, *Journal of Physical Chemistry C* 111 (2007) 18288–18293.
- [26] Q.J. Xiang, J.G. Yu, M. Jaroniec, *Chemical Society Reviews* 41 (2012) 782–796.
- [27] K.F. Zhou, Y.H. Zhu, X.L. Yang, X. Jiang, C.Z. Li, *New Journal of Chemistry* 35 (2011) 353–359.
- [28] V. Štengl, D. Popelková, P. Vlášil, *Journal of Physical Chemistry C* 115 (2011) 25209–25218.
- [29] Y.Y. Liang, H.L. Wang, H.S. Casalongue, Z. Chen, H.J. Dai, *Nano Research* 3 (2010) 701–705.
- [30] R. Leary, A. Westwood, *Carbon* 49 (2011) 741–772.
- [31] I.V. Lightcap, T.H. Kosel, P.V. Kamat, *Nano Letters* 10 (2010) 577–583.
- [32] M.S. Zhu, P.L. Chen, M.H. Liu, *Acs Nano* 5 (2011) 4529–4536.
- [33] H. Zhang, X.F. Fan, X. Quan, S. Chen, H.T. Yu, *Environmental Science and Technology* 45 (2011) 5731–5736.
- [34] G. Li, T. Wang, Y. Zhu, S.Y. Zhang, C.J. Mao, J.Y. Wu, B.K. Jin, Y.P. Tian, *Applied Surface Science* 257 (2011) 6568–6572.
- [35] H.D.a.Y.S. Yanyuan Wen, *Nanoscale* 3 (2011) 4411–4417.
- [36] R. Kenta, H. Kato, H. Kobayashi, A. Kudo, *Physical Chemistry Chemical Physics* 5 (2003) 3061–3065.
- [37] W.S. Hummers, R.E. Offeman, *Journal of the American Chemical Society* 80 (1958) 1339.
- [38] C. Nethravathi, M. Rajamathi, *Carbon* 46 (2008) 1994–1998.
- [39] Y.B. Chen, D.Z. Li, M. He, Y. Hu, H. Ruan, Y.M. Lin, J.H. Hu, Y. Zheng, Y. Shao, *Applied Catalysis B: Environmental* 113–114 (2012) 134–140.
- [40] W.J. Li, D.Z. Li, Y.M. Lin, P.X. Wang, W. Chen, X.Z. Fu, Y. Shao, *Journal of Physical Chemistry C* 116 (2012) 3552–3560.
- [41] L. Ge, J. Liu, *Applied Catalysis B: Environmental* 105 (2011) 289–297.
- [42] L. Ge, C.C. Han, J. Liu, *Applied Catalysis B: Environmental* 108 (2011) 100–107.
- [43] W. Li, D. Li, S. Meng, W. Chen, X. Fu, Y. Shao, *Environmental Science and Technology* 45 (2011) 2987–2993.
- [44] Y.H. Zhang, Z.R. Tang, X.Z. Fu, Y.J. Xu, *Acs Nano* 4 (2010).
- [45] J.G. Yu, L.J. Zhang, B. Cheng, Y.R. Su, *Journal of Physical Chemistry C* 111 (2007) 10582–10589.
- [46] W.G. Wang, J.G. Yu, Q.J. Xiang, B. Cheng, *Applied Catalysis B: Environmental* 119 (2012) 109–116.
- [47] W.J. Ren, Z.H. Ai, F.L. Jia, L.Z. Zhang, X.X. Fan, Z.G. Zou, *Applied Catalysis B: Environmental* 69 (2007) 138–144.
- [48] R. Asahi, T. Morikawa, T. Ohwaki, K. Aoki, Y. Taga, *Science* 293 (2001) 269–271.
- [49] Y.M. Lin, D.Z. Li, J.H. Hu, G.C. Xiao, J.X. Wang, W.J. Li, X.Z. Fu, *Journal of Physical Chemistry C* 116 (2012) 5764–5772.
- [50] A.H. Ye, W.Q. Fan, Q.H. Zhang, W.P. Deng, Y. Wang, *Catalysis Science and Technology* 2 (2012) 969–978.
- [51] N.J. Bell, H.N. Yun, A.J. Du, H. Coster, S.C. Smith, R. Amal, *Journal of Physical Chemistry C* 115 (2011) 6004–6009.
- [52] S.F. Chen, W. Zhao, W. Liu, H.Y. Zhang, X.L. Yu, Y.H. Chen, *Journal of Hazardous Materials* 172 (2009) 1415–1423.
- [53] J.X. Wang, H. Ruan, W.J. Li, D.Z. Li, Y. Hu, J. Chen, Y. Shao, Y. Zheng, *Journal of Physical Chemistry C* 116 (2012) 13935–13943.
- [54] A. Takai, P.V. Kamat, *Acs Nano* 5 (2011) 7369–7376.
- [55] W.H. Leng, Z. Zhang, J.Q. Zhang, C.N. Cao, *Journal of Physical Chemistry B* 109 (2005) 15008–15023.
- [56] T. Hirakawa, Y. Nosaka, *Langmuir* 18 (2002) 3247–3254.
- [57] H. Bader, V. Sturzenegger, J. Hoigné, *Water Research* 22 (1988) 1109–1115.
- [58] W.J. Li, D.Z. Li, W.J. Zhang, Y. Hu, Y.H. He, X.Z. Fu, *Journal of Physical Chemistry C* 114 (2010) 2154–2159.
- [59] R. Palominos, J. Freer, M.A. Mondaca, H.D. Mansilla, *Journal of Photochemistry and Photobiology A* 193 (2008) 139–145.